Evolution of Lateral Structures during the Functional Stack Build-up of P3HT:PCBM-Based Bulk Heterojunction Solar Cells

Shuai Guo,[†] Matthias A. Ruderer,[†] Monika Rawolle,[†] Volker Körstgens,[†] Christopher Birkenstock,[†] Jan Perlich,[‡] and Peter Müller-Buschbaum[†,*]

[†]Lehrstuhl für Funktionelle Materialien, Physik-Department, Technische Universität München, James-Franck-Strasse 1, 85748 Garching, Germany

[‡]Deutsches Elektronen-Synchrotron (DESY), Notkestrasse 85, 22603 Hamburg, Germany

ABSTRACT: Bulk heterojunction (BHJ) solar cells from 1,2-dichlorobenzene solution processed regioregular poly(3-hexylthiophene-2,5-diyl) (P3HT): phenyl-C61-butyric acid methyl ester (PCBM) are prepared and investigated at different steps of the multilayer stack build-up of the device. The inner structure is probed from the molecular to the mesoscale with grazing incidence small/wide-angle X-ray scattering (GISAXS/GIWAXS) and X-ray reflectivity (XRR). The surface morphology is detected with atomic force microscopy (AFM). Therefore, an in-depth knowledge of the three-dimensional morphology of the bulk heterojunction solar cell, starting from the cleaned ITO substrate up to the final post-treated solar cell, is generated. The active layer structure is influenced by the annealing as well as by the top contact deposition. Structures coarsen during the evaporation of the metal contacts. The P3HT crystal structure strongly depends on the device processing as well. These morphological changes together with the diffusion of aluminum atoms to the active layer are of importance for the device efficiency.

KEYWORDS: organic solar cell, morphology, P3HT:PCBM, GISAXS, GIWAXS
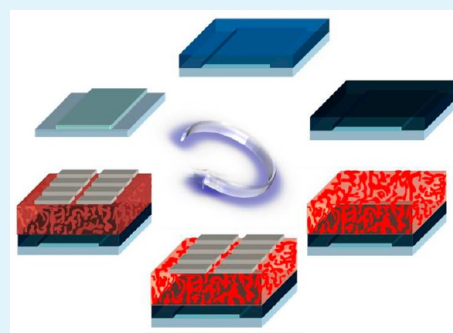
1. INTRODUCTION

The steadily increasing worldwide energy consumption as well as the detrimental effects on the environment and climate resulting from the combustion of fossil fuels have generated a strong interest in renewable solar energy sources. Although the power conversion efficiency of the monocrystalline photovoltaic cells have reached relatively high values (e.g., 20% under standard condition AM 1.5, 1 kW/m²),[1] inorganic photovoltaic devices are still costly and rigid.[2] The rapid progress in organic photovoltaic, originating from the concept of bulk heterojunction (BHJ) solar cells, opens up promising possibilities for industrialization and commercialization, because of the potential low production cost, the possibility of mechanical flexibility, the lightweight properties, and a similar theoretical power conversion efficiency (PCE) as compared with commercialized silicon-based solar cells (at about 15%).[3−5]

In general, polymer-based BHJ solar cells make use of a self-assembly phase separation of an electron-donating polymer blended with an electron-accepting material (fullerene, polymer, or oxide).[6,7] The electron-donating polymer[8−10] typically is a conjugated polymer, which offers the possibility of ultrafast charge transfer to the electron acceptor. Moreover, most of the incoming light is absorbed because of the high absorption coefficient of the polymer.[11] Organic BHJ photovoltaic devices have made great progress in the last years. In this research field, thorough investigations have been performed, including the material design, device architecture design, the choice for solvent, thermal or solvent annealing, etc.[12−19] In most cases, the ultimate

aim is to obtain an ideal morphology of the active layer. In a simplified approach, this ideal morphology of the BHJ blend consists of a bicontinuous interpenetrating nanoscale network of the electron donor and acceptor material. The nanoscale network offers a large interface area, and therefore a high exciton dissociation rate. The main energy conversion process, from light to electrical energy, takes place within this morphology. Excitons are generated when photons are absorbed by the active thin film, and dissociate at the interface between donor and acceptor material. Because of the different electron affinity, the separated free charge carriers are transported through each individual favorable phase and collected by the electrodes. The general guideline is that a careful balance between the amount of the interfacial area and the optimal size of the percolation paths (on the order of 10 nm) has to be achieved.[11,13,20−24] After intense efforts to obtain this optimized morphology within the thin films, the PCE of polymer solution-based solar cells has been improved up to more than 10%.[25,26] However, besides the progress in the total PCE of organic solar cells, an in-depth understanding of the morphologies installed during the complex build-up of the functional stack will be beneficial for further improvements. In particular, so far many investigations on the morphology are limited to the active layer of the BHJ device and do not take into account the complex architecture of the full device.[27−29]

Recently, Shao et al. reported on both nanoscale phase-separation and increased face-on orientation of the P3HT crystallites, by replacing PEDOT:PSS with p-type CuI, which highlights the significance of interface engineering in organic solar cells.[30] Kim et al. demonstrated that the characteristic properties of the organic layer, e.g., morphology, thickness, interface engineering can effectively influence the FF of organic photovoltaic cells.[31] Chen et al. also reported that morphology and interfacial behavior between active layers and electrodes are strongly affected by the preparation conditions.[32] Tillack observed that the changes in device performance as a result of substrate modification are mainly due to the buried substrate/film interface instead of the exposed film/air interface.[33] Therefore, in this article for the first time we focus on the evolution of morphologies, which are generated during the build-up of the functional stack of the solar cell.

Recently, Perlich et al. demonstrated the possibilities of advanced X-ray scattering to track the evolution of morphologies of a multilayer stack built-up of self-encapsulated thin titania films with application in organic photovolatics.[34] A fabrication process which allows the preservation of an initially tailored nanostructure was reported, which is of great importance for hybrid solar cells. In the present investigation, we focus on the polymer:fullerene (P3HT:PCBM) BHJ system, which is among the most investigated systems in organic photovoltaic research. Changes in the structure of the BHJ morphologies are tracked as a function of a multilayer stack built-up via the same advanced X-ray scattering technique, namely grazing incidence small-angle X-ray scattering (GISAXS), as used by Perlich et al.[34] Grazing incidence wide-angle X-ray scattering (GIWAXS), X-ray reflectivity (XRR) and atomic force microscopy (AFM) complement the investigation of the structure. P3HT and PCBM are deposited out of 1,2-dichlorobenzene because the used solvent is important for the installed morphology.[35] Huang et al. demonstrated that the film drying process is critical to the final device performance for high boiling point solvents such as 1,2-dichlorobenzene.[36] The high boiling point and therefore a slow evaporation speed are beneficial for the initial morphology creation.[8,37]

2. EXPERIMENTAL SECTION

a. Materials. The polymer to prepare the solar cell is regioregular poly(3-hexylthiophene-2,5-diyl) (P3HT), acting as an electron donor (purchased from Rieke Metal. Inc. and used as supplied). The average molecular weight, density, and regioregularity are about 50 kg/mol, 1100 kg m^{-3},[38] and 95%, respectively. The electron acceptor material is the fullerene derivative 6,6-phenyl-C61 butyric acid methyl ester (PCBM) which is synthesized and purchased from Nano-c with a purity of 99.5%. Poly(3,4-ethylenedioxythiophene):poly(styrenesulfonate) (PEDOT:PSS) as received from Sigma Aldrich is a transparent blend of two polymers, PEDOT and PSS, dispersed in H_2O. It is used as electron blocking layer in the device.

b. Sample Preparation. All samples are prepared on glass-ITO substrates, purchased from SOLEMS S.A. with the size of 2.2×2.2 cm^2. The substrates are patterned by chemical etching and cleaned with alconox solution and several organic solvents in an ultrasonic bath (ethanol, acetone, and isopropanol - one after another). Between each step the substrates are rinsed with the solvent just being used and blown dry with nitrogen gas. Oxygen- plasma treatment is performed on the cleaned ITO substrates for 10 min to increase the hydrophilicity of the surface before spin-coating of the PEDOT:PSS films. The PEDOT:PSS solution is dissolved by putting it in an ultrasonic bath for 10 min. Afterward, it is filtered through PTFE filters (5 μm) and spin-coated for 60 s at 3000 rpm rotation speed (Süss MicroTec Delta 80 spin-coater) under ambient conditions (temperature: 18 °C, humidity: 32%). The

obtained PEDOT:PSS layer can be regarded as a high work-function metal.[39] This electron blocking layer is annealed at 150 °C for 10 min in air to remove the residual water before spin-coating of the P3HT:PCBM active layer. To prepare the P3HT:PCBM blend film, the PCBM powder is first dissolved in 1,2-dichlorobenzene until complete dissolution, and then the required amount of pristine PCBM solution is added to the dissolved P3HT with the concentration of 60 mg mL^{-1} at the ratio of 0.8:1. This solution is stirred overnight to achieve better uniformity. A homogeneous active layer is deposited by spin-coating. The parameters of acceleration and rotation time are set to 9 and 30 s with the rotation speed of 2000 rpm. The devices are completed by a thermal deposition of a layer of aluminum at vacuum conditions (3.8×10^{-5} mbar). The deposition process is monitored by a quartz crystal ratemeter purchased from Inficon. The deposition rate starts with 0.1 Å/s and speeds up to 20 Å/s till the film thickness reaches 100 nm. Finally, an annealing treatment (140 °C for 10 min) of the whole device in nitrogen atmosphere is performed, as it is reported that 140 °C is an optimal annealing temperature for the P3HT:PCBM BHJ solar device.[40] The effective area of the devices is determined by the overlap of aluminum and ITO electrodes to 15 mm^2. For each piece of glass-ITO substrate, eight pieces of effective area (pixels) are prepared.[41]

c. Measurements. The investigation involves real-space imaging techniques such as atomic force microscopy (AFM) and reciprocal space techniques such as X-ray reflectivity (XRR) and grazing incidence small/wide-angle X-ray scattering (GISAXS/GIWAXS).

Current−Voltage Characterization. The performance of the solar cell devices is characterized under AM1.5 illumination, and recorded as IV curves with a source meter (Keithley 2400). Before the measurement of the efficiency, a reference cell is used to calibrate the solar spectrum to the standard 1.5AM radiance with an intensity of 1000 W/m^2.

Atomic Force Microscopy (AFM). An Autoprobe CP Research AFM instrument is used to get the two-dimensional topography images in the noncontact mode to minimize the tip-induced damage to the soft polymer films. Each image consists of 256 lines where each line contains 256 data points.

X-ray Reflectometry. X-ray reflectivity (XRR) measurements are performed on a Siemens D5000 diffractometer at a wavelength of 0.154 nm (Cu−Kα radiation) within the angular range from 0° to 8°. A point detector is used to record the reflected intensity. The detector is protected by an auto beam absorber. Film thickness information is obtained by fitting the reflectivity data with software Parratt.

GISAXS. The GISAXS measurements are done at the synchrotron beamline BW4, HASYLAB (DESY) in Hamburg, Germany.[42] A wavelength of $\lambda = 0.138$ nm and an X-ray beam with a size of 23×36 μm^2 are selected. The scattered intensity is collected with a MarCCD detector. Due to the high intensity of the directly transmitted and the specularly reflected beam, two moveable beamstops are used to protect the detector. To allow for an excellent sampling statistics at large q_y values, a rod-shaped beamstop replaces the point-like beamstops in measurements with long data acquisition time to block all intensity at $q_y = 0$. The vertical cuts are performed on those GISAXS data collected with point-shaped beamstops. The individual sample is placed on a goniometer and a constant incident angle ($\alpha_i = 0.495°$) is used for all samples. Because the critical angles of the investigated polymers (0.13−0.16°) and the aluminum electrodes (0.21°) are smaller than this incident angle, both surface and inner film structures are probed. The sample−detector distance (SDD) is 2.035 m. To get precise structure information, horizontal and vertical cuts of the 2D GISAXS data are performed (referring to the sample surface). The vertical cut at the position $q_y = 0$ gives structure information perpendicular to the substrate. The horizontal cut at the critical angle of each material contains the lateral structure properties such as the size of phase domains, distribution, etc. To model all the intensity distribution of horizontal cuts, the so-called effective interface approximation is used to determine the most prominent in-plane length scales.[43]

GIWAXS. GIWAXS measurements are performed at beamline BW4 as well.[44] To record crystalline structures, we reduced the SDD to 0.10 m. Sector integrals replace the line cuts.

3. RESULTS AND DISCUSSION

To follow the evolution of the characteristic structures during the functional stack build-up, individual samples are prepared and analyzed for selected steps of this build-up. These investigated samples and the corresponding preparation process steps are schematically presented in Figure 1. Like for all photovoltaic
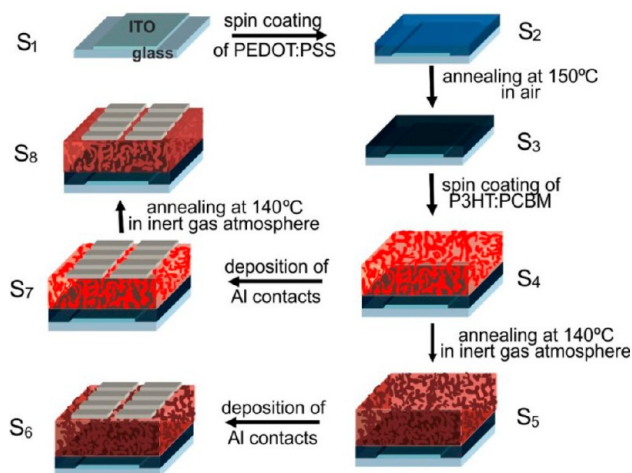

Figure 1. Scheme of the individual steps S_1 to S_8 of the functional stack build-up for the P3HT:PCBM-based BHJ solar cell used in the present investigation.

devices, multiple layers are sandwiched between two electrodes. In the type of polymer-based BHJ solar cell under investigation, a thin transparent layer of indium tin oxide (ITO) works as the anode at the bottom while an aluminum layer is used as the cathode on the top. In between, the PEDOT:PSS blocking layer and an active layer consisting of a mixture of P3HT and PCBM are spin-coated, respectively.[45] A well-suited polymer blend film thickness is achieved by adjusting the solution concentration and all parameters of the spin-coater. Annealing of the active layer in an inert gas atmosphere is done before or after evaporation of the aluminum electrode on top. The annealing step facilitates the self-organization of the polymer and increases the crystallinity of the film. Self-organization could improve the field-effect carrier mobility in RR-P3HT by a factor of 100 to 0.1 cm^2 V^{-1} s^{-1}, leading to a higher free charge transportation coefficient.[45]

To summarize, sample S_1 denotes the chemically etched and precleaned ITO substrate, as-spun PEDOT:PSS on top of the ITO substrate corresponds to sample S_2, annealing of sample S_2 as described in Figure 1 results in sample S_3. Sample S_4 results from spin-coating P3HT:PCBM (the active layer) on top. Annealing the multilayer in nitrogen atmosphere gives sample S_5, and the thermal evaporation of aluminum top contacts leads to sample S_6. To investigate the effects of diffusion of aluminum into the active layer and annealing, sample S_7 denotes the as-prepared solar cell device without any pre- or post-treatment (top contact directly on sample S_4), and annealing this device (postannealed solar cell) defines sample S_8.

3.1. Solar Cell Performance. The as-prepared and annealed solar cell devices (samples S_6, S_7, and S_8) are tested concerning their photovoltaic performance by measuring $I-V$ curves as shown in Figure 2.

The device performance of organic solar cells are characterized mainly by three parameters: short circuit current I_{sc}, open circuit voltage V_{oc}, and fill factor FF, which is the ratio of the maximum obtained power to the product of I_{sc} and V_{oc} of the solar cell (see
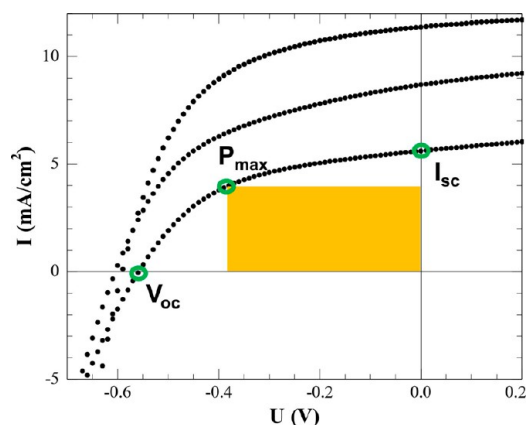

Figure 2. $I-V$ curves of the as-spun (S_7, bottom curve), the preannealed (S_6, middle curve), and the postannealed solar cells (S_8, top curve).

figure 2).[46] Comparing the as-prepared sample (S_7) with the one annealed after evaporation (S_8), I_{sc} increases dramatically from 5.61 to 11.37 mA/cm^2 as listed in Table 1. In contrast, for the

Table 1. Parameters of Solar Cells Devices: as-spun (S_7), pre-annealed (S_6) and post-annealed (S_8)

sample	$I_{sc}(mA/cm^2)$	$V_{oc}(V)$	FF (%)	$\eta(\%)$
S_7	5.61	−0.56	48.5	1.52
S_6	8.69	−0.60	48.4	2.54
S_8	11.37	−0.59	53.7	3.61

sample annealed before aluminum is thermally evaporated on top (S_6), I_{sc} improves by 55% to 8.69 mA/cm^2. Therefore, the efficiencies improve via annealing as known from literature.[11] V_{oc}, however, remains constant for all the solar cells as is expected at 0.58 ± 0.2 V, because it is determined by the difference between the HOMO of the donor and the LUMO of the acceptor material.[11] The fill factor of the postannealed sample (S_8) is the highest with a value of 53.7%, whereas the preannealed one is the lowest with only 48.4%. Therefore, for the solar cell that is thermally treated before the aluminum is thermally evaporated on top of P3HT:PCBM layer, shows a lower PCE (2.54%) as compared with the one prepared the other way around (3.61%).

3.2. Mesoscopic Structure. To probe the mesoscopic structure of the individual samples the multilayer stack build-up is characterized with grazing incidence small-angle X-ray scattering (GISAXS). GISAXS offers not only the structure information about the film surface such as roughness correlations,[47] but also gives access to the inner film morphology in terms of lateral structures, size distributions, and spatial correlations. All these advantages, together with the excellent statistics, make GISAXS an excellent choice to track the changes of the morphology inside the functional stack. In addition to the thickness of laterally correlated layers D_c, the smallest replicated in-plane length scale R_c is accessible.[47]

A scheme of the used GISAXS geometry is displayed in Figure 3a. The incident X-ray beam with a wave vector k_i impinges on the sample surface, and a two-dimensional (2D) detector collects the scattered intensity. The directly reflected X-ray beam has to be shielded with a beamstop in front of the detector to protect the detector due to its high intensity. Thus, the brightest data points in the 2D GISAXS data are caused by the Yoneda peak, which occurs when the incident angle is equal to the critical angle
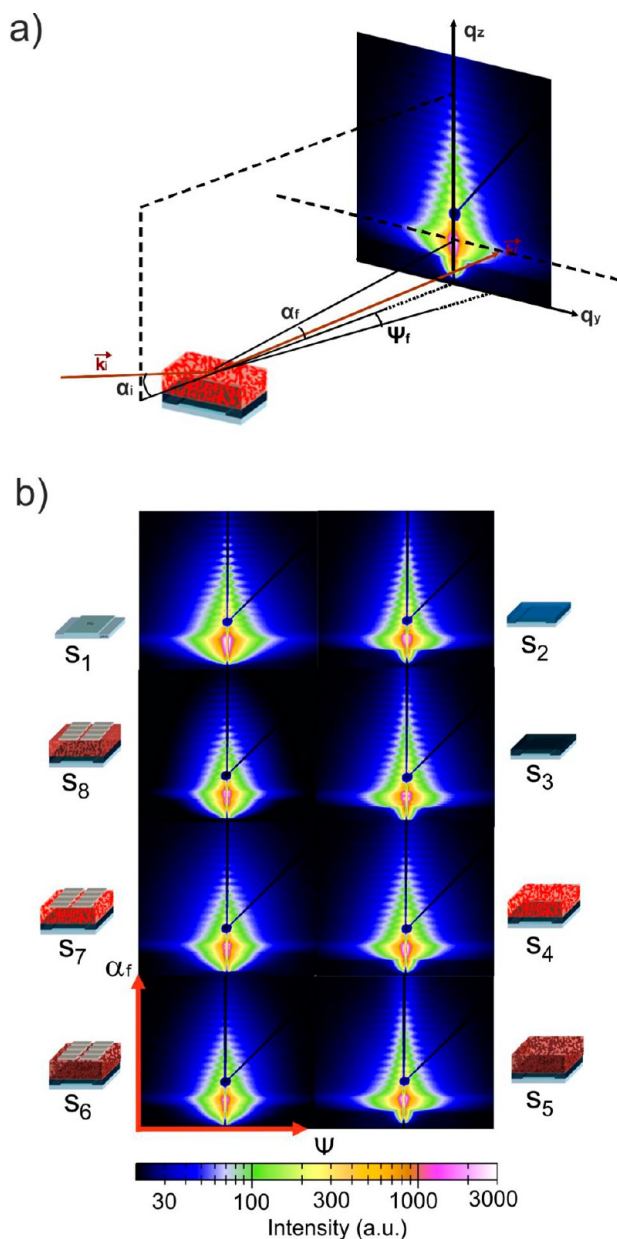
Figure 3. (a) Scheme of the GISAXS geometry: The sample is mounted horizontally on a sample holder. The X-ray beam impinges on the sample surface with a fixed incident angle α_i, is reflected with the same exit angle and shielded with a beamstop. The scattered X-ray beam with an exit angle α_f and the in-plane angle Ψ yields the intensity distribution of the GISAXS data. (b) Composition of the serial 2D GISAXS data displayed as the function of the device build-up. In each individual image, the exit angle of the X-ray beam α_f is plotted on the y-axis and the in-plane angle Ψ at the x-axis. The intensity is shown on logarithmic scale. Along with the 2D GISAXS data, the corresponding stage of the functional stack build-up is sketched.

α_c of the investigated materials and the transmission functions have a maximum value.[48]

In Figure 3b, the 2D GISAXS data are presented as a function of the different steps of the solar cell build-up. Different colors represent different intensities as indicated by the color bar. For each 2D GISAXS data the x-axis is the so-called in-plane angle ψ, which contains the lateral structure information. The vertical structure information is extracted along the y-axis, defined as the exit angle α_f.

3.2.1. Mesoscopic Structure along the Surface Normal. In Figure 4, the vertical cuts from the 2D GISAXS data are
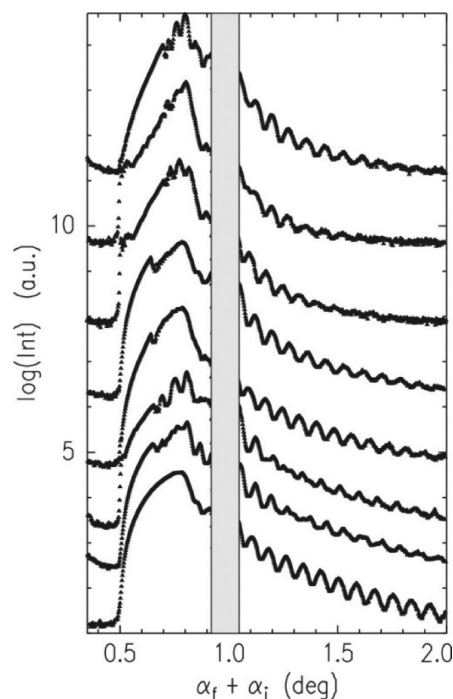

Figure 4. Vertical cuts of the 2D GISAXS intensity shown as a function of the detector angle $\alpha_i + \alpha_f$ for the different steps of the functional stack build-up (S_1 to S_8 from bottom to top). The beamstop is indicated by the gray box. For clarity, the curves are shifted along the intensity axis.

presented for all the individual steps of the functional stack build-up (samples S_1 to S_8). In all curves a drop in intensity is caused by the shielding with a beamstop at the position of the specularly reflected beam ($\alpha_i = \alpha_f$), thereby allowing to separate the scattered intensity in two parts with respect to this shielding. On the left side of the shielded region (small detector angles $\alpha_i + \alpha_f < 1°$), the intensity is dominated by the Yoneda peak.[48] The Yoneda peak corresponding to the ITO material shows up in all vertical cuts. With addition of further layers to the functional stack, additional Yoneda peaks occur, arising from PEDOT:PSS (second and third curve from bottom) and P3HT:PCBM (fourth and fifth curve from bottom), as well as aluminum. The large roughness of the P3HT:PCBM layer makes the corresponding Yoneda peak so pronounced that the ones from the PEDOT:PSS are no longer visible. No big change happens due to the annealing. With deposition of aluminum on top, a complicated scattering signal reestablishes (see sample S_6). The first peak from the left is ascribed to aluminum. It remains constant in the same position for the other two samples with aluminum top contacts. Because it is buried under the aluminum layer, the P3HT:PCBM features get less pronounced but are still present. It is concluded from a global comparison of the Yoneda region of all the vertical cuts, that each material within the functional stack exhibits its own feature at a different angular position, for instance at the critical angles $\alpha_c = 0.13$, 0.14, and 0.21° for PEDOT:PSS, P3HT, and aluminum, respectively. On the right side of the shielded region in the vertical cuts (large detector angles $\alpha_i + \alpha_f > 1°$), periodic oscillations are present for all curves due to resonant diffuse scattering, originating from a rough and laterally disordered ITO film (see Figure 4).[49] For the samples S_2 and S_3 thickness interference between the ITO and the

PEDOT:PSS layer occurs, giving rise to a more complex intensity decay. Similar but weaker periodic oscillation signal for the samples S_6 and S_7 is observed, coming from a smeared interface between the active layer and the aluminum layer. Because postannealing treatment improves the interfacial connection for all the interfaces, the pronounced oscillations caused by correlated thickness are reestablished for sample S_8.

From the intensity oscillations in the vertical cuts, the information about correlated thickness is extracted. Using the simple approach $D_c = 2\pi/\Delta q$ and $\Delta q = (2\pi/\lambda)\sin(\Delta\alpha)$, in which $\Delta\alpha$ is the averaged angular distance between two adjacent intensity maxima in the vertical cuts, the correlated thickness is calculated.[49] The corresponding values are displayed in Figure 5a. Within the experimental error for all different samples similar
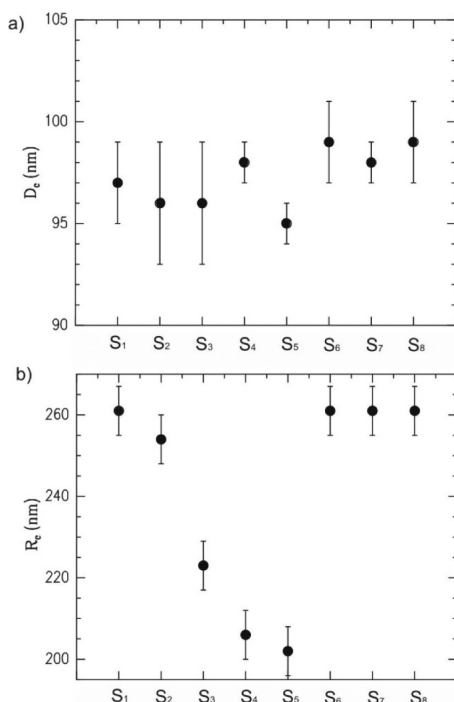

Figure 5. (a) Correlated thickness D_c and (b) smallest replicated in-plane length scale R_c as a function of the stack build-up labeled by the respective abbreviation from S_1−S_8.

values are obtained. For sample S_1 this can be unambiguously ascribed to the ITO layer with a thickness of (97 ± 2) nm. For the samples S_2 to S_5 it is very likely that the correlated layer is still dominated by the ITO layer, because the other added layers (PEDOT:PSS and P3HT:PCBM) differ in thickness. For the samples S_6 to S_8 the thickness of the aluminum layer matches the correlated thickness again. It was shown in a previous investigation, that the aluminum contact exhibits same correlation.[50] Therefore we attribute the observed interface correlation for these samples (S_6 to S_8) to the aluminum electrode. Furthermore, the smallest replicated in-plane length scale R_c is determined from the 2D GISAXS data as a function of the stack build-up by performing off-centered vertical cuts. The off-centered vertical cut without intensity modulation corresponds to the critical lateral wave vector components q_c for which the interfaces scatter independently.[47] The determined R_c values are plotted in Figure 5b. The rough ITO surface has a value of 260 nm. With the addition of the next layers this value decreases, meaning that smaller in-plane lengths are correlated. Because we

assign the interface correlation to the ITO layer, the ITO surface is modified by the spin-coating of PEDOT:PSS, by the annealing and the deposition of the active layer. For the samples S_6 to S_8, increased values of R_c manifests that the aluminum layer cannot replicate the structures of the underneath layers that well, independent of the processing conditions.

By employing XRR measurements, additional vertical film composition is available. As most properties of photovoltaic films are thickness dependent, the determination of the film thickness with a high precision is of utmost interest. Additionally, the surface and interface roughness and the scattering length densities are accessible. In Figure 6 the XRR data of sample S_2
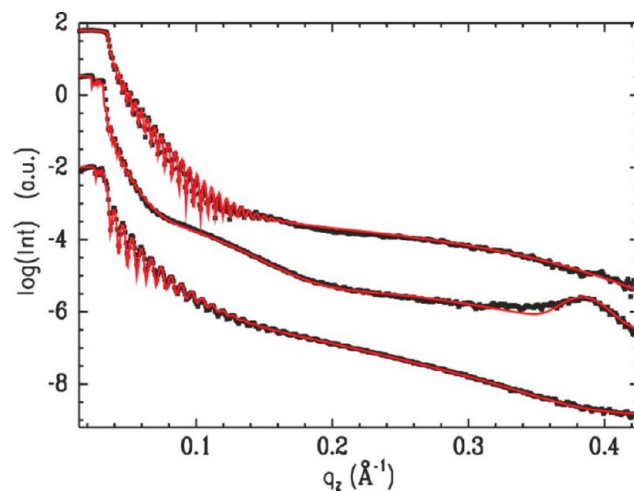

Figure 6. XRR data (dots) shown together with a model fit (lines) of the PEDOT:PSS layer, the active P3HT:PCBM layer, and the aluminum layer (plotted from bottom to top).

(the PEDOT:PSS layer), sample S_4 (with the added active P3HT:PCBM layer), and sample S_6 (with the aluminum layer) are shown as examples. We use a Parratt algorithm for fitting (as indicated by red solid lines in Figure 6). A multilayer model including thickness, scattering length density, and roughness between the layers is applied in the algorithm. By iterative comparison of the fitting data with the measured reflectivity, the vertical material profiles are extracted. For the investigated functional stacks, the accurate thickness of the PEDOT:PSS, the P3HT:PCBM active layer as well as the aluminum layer are 80, 155, and 105 nm, respectively.

Having a thickness similar to the ITO layer thickness gives rise to the complicated intensity oscillations in the detector cuts as described before. Regarding the active layer deposited by spin coating, it is typically difficult to extract charges from a device thicker than 200 nm,[51] which makes an optimal thickness of the active layer another significant factor for the device performance. Recent work showed that with alternative deposition techniques such as spray coating thicker active layers can give rise to high PCE values.[52,53] In our case, the selected thickness of the P3HT:PCBM layer of 155 nm is a good compromise between absorbing more sunlight and producing more photocurrent according to our experience with spin coated active layers. With a thickness of the P3HT:PCBM layer larger than the thickness of the PEDOT:PSS or the ITO layer underneath and moreover with a large surface roughness of the P3HT:PCBM film, the intensity oscillations weaken in the GISAXS data of sample S_3. In addition, a PCBM enriched layer is present at the bottom of the P3HT:PCBM blend layer, as observed in the scattering length
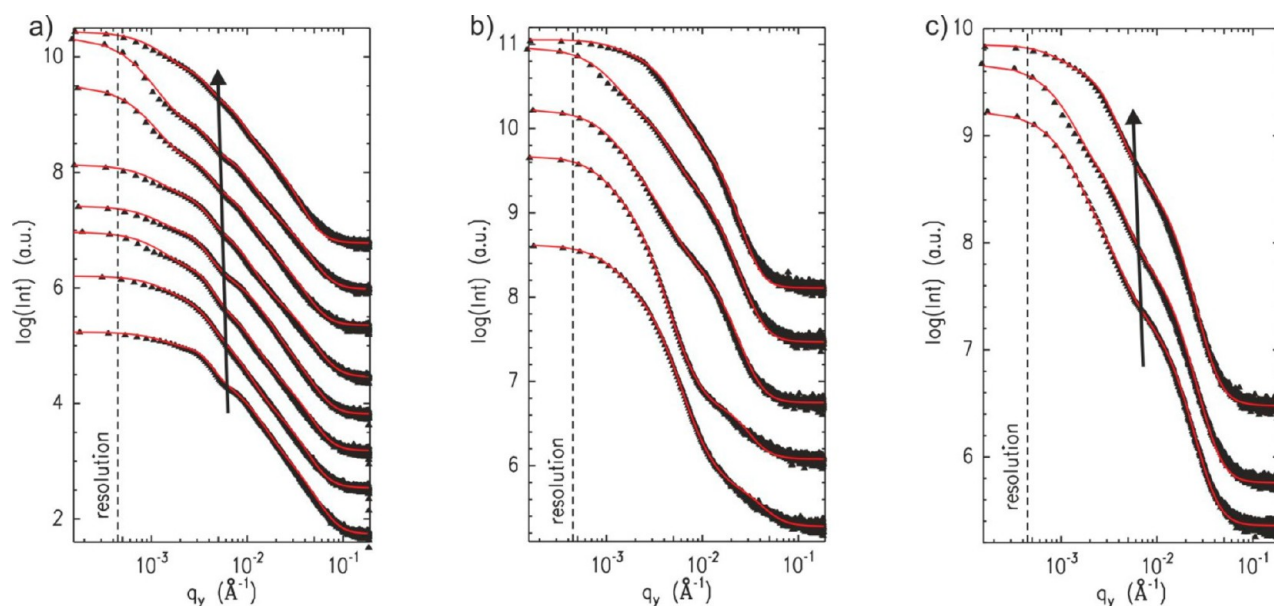
Figure 7. Double-logarithmic plots of the horizontal cuts from the 2D GISAXS data (dots) at the critical angles of (a) ITO (from S_1 to S_8), (b) P3HT (from S_4 to S_8), and (c) aluminum (from S_6 to S_8). Solid lines are fits as explained in the text. The arrows in graphs a and c represent constant structures of 105 nm for ITO and 95 nm for aluminum, respectively. For clarity, the curves are shifted along the intensity axis.

density profile. Above this ultrathin PCBM enriched layer, a relatively thick mixture layer (the BHJ layer) is present. This kind of vertical gradient is unfavorable to generate a higher photocurrent, because all the separated free holes will recombine within this electron accepting ultra-thin PCBM layer, leading to lower device performance. A more ideal configuration would be an additional ultrathin P3HT layer located between PE-DOT:PSS layer and the active layer, and an enriched PCBM layer on top.[54] In the XRR data, the intensity modulation is strongly damped because of the surface roughness of the active layer which is formed via spin-coating. This roughness is beneficial for a reduced light reflection and can result from the high viscosity of the solvent and the very high concentration of the polymer solution used during spin-coating. The thickness of the aluminum contacts for all three samples is 105 nm. Thickness of aluminum electrode about 100 nm is commonly used for organic BHJ solar cells, which is the optimal thickness as cathode.[36,55]

3.2.2. Mesoscopic Lateral Structure. Information about lateral structures is obtained from the analysis of the horizontal line cuts of the 2D GISAXS data at the critical angles of each investigated material (ITO, PEDOT:PSS, P3HT or PCBM, and aluminum). At the corresponding critical angle the horizontal cut is most sensitive to material related structure information due to the Yoneda peak enhancement.[56] In Figure 7, the horizontal cuts are plotted as a function of the lateral scattering vector component q_y for ITO, P3HT, and aluminum, respectively. All curves are shown in the order of the preparation steps to assemble the solar cell from bottom to top. Data for PEDOT:PSS are not shown as they do not exhibit particular features. Weak features in the GISAXS signals are common for P3HT:PCBM films because of the size distribution and distance distribution of the PCBM domains inside the P3HT film.[36,54,57]

All horizontal cuts are fitted with the effective interface approximation model within the distorted-wave Born approximation (DWBA), assuming form and structure factor contributions.[43] It should be noted, that an alternative approach for modeling GISAXS data of an active layer of P3HT:PCBM

makes use of Debye–Anderson–Brumberger equation (DAB model), which describes the scattering of a randomly distributed (nonparticular) two-phase polymer system in terms of correlation length (a measure of the average spacing between phase regions).[58] On the basis of the DAB model, Liao and co-workers characterize the large scale network of PCBM molecules distributed within the amorphous and around the crystalline P3HT molecular conformations.[59] However, as we model structural information from a functional stack consisting of different layers, we selected the simpler approach. Qualitatively, the characteristic structure sizes of ITO are preserved during the solar cell device assembling process. The calculated characteristic lateral length for ITO is $\Lambda_a = 105$ nm (shown by the arrow in Figure 7a). The morphology of the ITO layer stays unchanged, which means that ITO with respect to its lateral structure is influenced neither by other materials on top nor by the annealing treatments afterward. The same is observed for the characteristic lateral structure of the aluminum layer, which has a value of $\Lambda_c = 95$ nm (shown by the arrow in Figure 7c). For both ITO and aluminum, only the intensities are affected by the different steps of the build-up, which can originate from changed contrast conditions of the GISAXS experiment because of the addition of further layers.[47]

In contrast to the ITO and the aluminum layer, changes occur in the lateral structure sizes of the active layer. In the horizontal cuts taken for P3HT (Figure 7b), peak positions shift for the different steps in the stack build-up. In Figure 8, the dominant in-plane lengths for ITO, P3HT, and aluminum, extracted from the fitting model based on the effective interface approximation, are summarized as a function of the assembling process. For PEDOT:PSS, no characteristic lateral structure is found.

Right after spin coating (sample S_4) in the P3HT:PCBM layer, the smallest in-plane structure is found with characteristic distances smaller than 50 nm. Because of annealing (sample S_5), the phase separation of P3HT and PCBM leads to a coarsening of structures. The deposition of the aluminum top contact (sample S_6) causes a further increase to 80 nm. In case the aluminum top contact is directly deposited on top of the as-
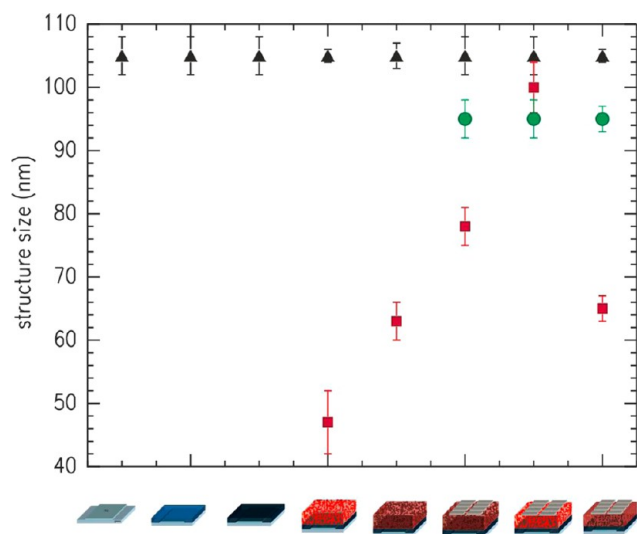
Figure 8. Extracted most prominent in-plane-length scale. The structure sizes of ITO (filled triangle), P3HT (filled square), and aluminum (filled circle) are plotted as a function of the stack built-up as indicated by the icons.

prepared P3HT:PCBM film (sample S_7) an even larger increase of the in-plane structure (100 nm) is observed. The thermal load applied during the top contact deposition might cause this additional coarsening of the lateral structures, which demonstrates that this step contributes significantly to the morphology of the active layer and cannot be neglected. Interestingly, a postannealing step (sample S_8) after top contact deposition results in a decrease of lateral structures, underlining that the presence of a top layer changes the interactions in the system. The value of 65 nm can explain the dramatic improvement of the power conversion efficiency of the solar cell after annealing. Therefore, PCE and the most prominent in-plane length scale are in good agreement along the common believe that smaller domain structures of the BHJ morphology cause higher efficiencies of the solar cells.[11,60]

To complete the picture of the three-dimensional morphology, AFM measurements are performed. As an example, the AFM topography data for four steps of the functional stack build-up are shown in Figure 9: the as-spun P3HT:PCBM film (sample S_4), the annealed P3HT:PCBM film (sample S_5), the as-spun solar cell (sample S_7), and the annealed solar-cell (sample S_8).

Directly after spin-coating, the P3HT:PCBM surface is rough (see figure 9a), which is consistent with the XRR measurements. After annealing, the surface roughness increases (see Figure 9b). The surface of the aluminum contact differs from the P3HT:PCBM surface. It appears grainier because of the small clusters of aluminum. Moreover, it is observed that the aluminum cluster size is comparable to that of the P3HT:PCBM film, which is in good agreement with the observed roughness correlation in the GISAXS data (see Figure 9c, d). Annealing of the solar cell causes no additional changes to the surface topography of the aluminum surface (Figure 9d).

To get more statistically relevant information about the surface structures, the power spectral density (PSD) is calculated from the AFM data of different scan ranges by performing a Fourier transformation and a radial average of the topography data. For the PSD curves shown in Figure 9e, AFM data with different scan sizes from $1 \times 1~\mu m^2$ to $8 \times 8~\mu m^2$ are combined.[61,62] The PSD curves show no pronounced features due to the absence of well-
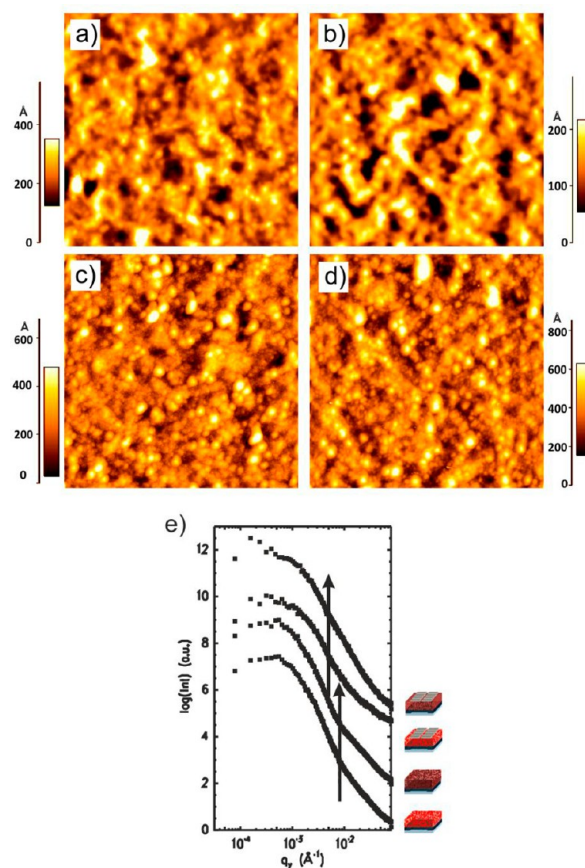

Figure 9. AFM topography data (scan size $4 \times 4~\mu m^2$) of four steps during the preparation process: (a) as-spun P3HT:PCBM (S_4), (b) annealed P3HT:PCBM (S_5), (c) as-spun P3HT:PCBM + Al (S_7), (d) annealed solar cell (S_8). Different color bars are used for the heights to illustrate the surface topography. (e) PSD calculated from the AFM topography data with different scan sizes from $1 \times 1~\mu m^2$ to $8 \times 8~\mu m^2$.

defined surface structures. The comparison between PSD curves resembling surface structures and GISAXS data probing inner film structures shows differences between both. The size of the domains present at the P3HT:PCBM film surface (80 nm, see arrow in Figure 9e) is bigger than the size of the domains inside the active layer. This difference is present for both, as-spun and annealed P3HT:PCBM films (samples S_4 and S_5). For the top contact (aluminum film) as well, the surface structure found with AFM (105 nm) is larger than the one probed with GISAXS (95 nm), regardless of annealing (for both samples S_7 and S_8). Anyhow, one needs to note the very limited statistics of the AFM investigation, as GISAXS averages over a significantly larger sample size.[56]

3.3. Molecular Order and Crystallinity. In addition to the mesoscopic structure, structure information on smaller length scales is of importance. For organic photovoltaic devices, it is crucial to have an optimized crystallinity and a preferred crystal orientation within the active layer to assist the charge transport.[11] To detect the crystallinity of P3HT and PCBM in the active layer, we performed grazing incidence wide-angle X-ray scattering (GIWAXS) measurements. By taking a vertical and horizontal sector integral from the 2D GIWAXS data, we obtain molecular orientation, polymer backbone spacing, and crystal sizes.[63,64]

As seen from Figure 10, crystalline structures are already found in all as-spun films (samples S_4 and S_7) with or without the presence of Al contacts, indicating that a first preordering of the
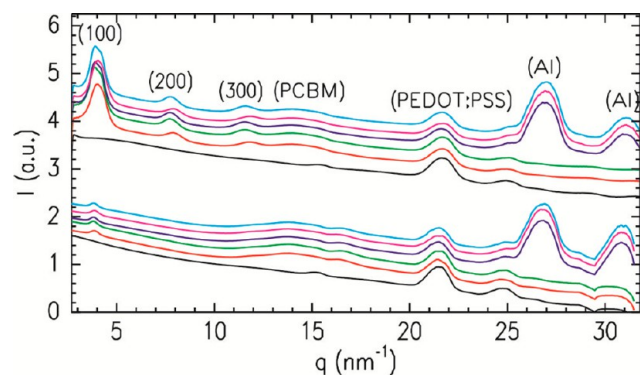
Figure 10. Horizontal (lower six curves) and vertical (upper six curves) sector integrals of 2D GIWAXS data of the samples as a function of the stack build-up from S_3 to S_8 (bottom to top). All curves are shifted along the y-axis for clarity of the presentation.

P3HT chains takes place already during the spin-coating process without thermal annealing. After thermal annealing, for all samples, the (100) Bragg peaks of P3HT shift to slightly lower q values, which implies that the backbone spacing increases after 10 min of thermal annealing. To obtain a quantitative analysis, all Bragg peaks are fitted with Gaussian functions, and lattice constants are extracted. The P3HT backbone spacing in the (100) direction increases from 1.55 to 1.59 nm for all thermally annealed samples, which is in agreement with investigations of crystallization on P3HT:PCBM system reported by Agostinelli et al.,[65] Moreover, thermal load caused by the top contact deposition can influence the P3HT crystal structure, depending on the sample history. In contrast, the lattice parameters always remain unchanged for PCBM during the whole functional stack build-up. Moreover, the (010) Bragg peak of P3HT is also weakly visible at about $q = 16.5$ nm^{-1}, manifesting the presence of the face-on orientation in the films, although the main crystal orientation is the edge-on configuration.

At $q = 21.5$ nm^{-1}, PEDOT:PSS Bragg peaks are detected, and the Bragg peaks at highest q values correspond to the presence of Al. Similarly, in the horizontal cuts three repeating features are observed: the P3HT (100) Bragg reflection at $q \approx 4$ nm^{-1}, the PCBM Bragg peak at $q \approx 14$ nm^{-1}, and the P3HT (010) Bragg peak at $q \approx 16.5$ nm^{-1}. However, the intensity of the P3HT (100) Bragg peaks is less pronounced as compared to the vertical cuts, whereas the (010) Bragg peak is comparatively stronger. This again confirms that both, face-on and edge-on crystal orientation exist in the P3HT films, and edge-on orientation is the prevailing configuration. In addition, by calculating the ratio of peak intensity between two different orientations, we can conclude that thermal annealing leads to more edge-on orientation and the presence of the Al contact disturbs the P3HT crystal alignment in the face-on configuration. In the horizontal cuts, the crystal size of PCBM stays rather constant during the stack built-up, as seen for PEDOT:PSS, and Al at higher q values as well.

As is well-known that an improved crystal size can dramatically improve the device performance, the crystallite size of P3HT is calculated from the Scherrer equation. To have a look at the effect of thermal annealing, the crystal sizes extracted from the samples S_4 (as-spun) and S_5 (thermal annealed) are compared. Without the presence of Al contacts a moderate increase from 6 to 7 nm is found in the (100) direction, which cannot fully address the difference of corresponding device performance. However, it may help to improve the charge carrier mobility to some extent. Ng et al. also found an increased order of P3HT

chains caused by annealing treatment, which is in agreement with our investigations.[66] Yu et al. suggested that thermal or solvent annealing could reduce the hole trap states in the regioregular P3HT:PCBM blend system, and therefore, improve the efficiency.[67]

For functional stacks with deposited Al contacts, pre- or postannealing gives rise to big differences in device performance. Besides the influence of the mesoscopic domain structure, a possible reason can be found in the applied annealing procedure. For the preannealed solar cell (sample S_6), the fast annealing and cooling procedure freeze-in the P3HT chain configuration within the bulk heterojunction film. Thus, the diffusion of Al atoms thermally evaporated afterward is reduced, as evident by the almost constant crystal size before and after deposition of the Al top contact. In comparison, the post-treatment allows original amorphous as-spun P3HT:PCBM film to grow P3HT crystallites more effectively because there is more free volume in the P3HT crystal, leading to an obvious change in crystal size (from 6 to 11 nm) after Al deposition.

An interlayer, formed by the diffusion of Al atoms into the active layer, plays an important role in improving the solar cell performance, as one can see from the solar cell efficiencies. Therefore, thermal annealing is a very crucial post-treatment step to enhance the device performance for the P3HT:PCBM system. It has been observed by Kim et al. that rapid heating and cooling increases the interlayer thickness more than a slow one.[68] It also has been reported by Kim et al. that the mesostructures of the organic films are strongly modified with the presence of Al electrode on top. An ultrathin (0.7 nm) face-on P3HT molecular stacking near the film surface in the absence of the Al electrode during thermal annealing disappeared in the presence of an Al electrode at P3HT:PCBM blending ratio 1:0.65, and the corresponding device performance is in agreement with our investigation.[69] Moreover, Kaune et al. detected via X-ray reflectivity the presence of a 2 nm thick intermixing layer at the Al:P3HT interface.[50] A layer of similar thickness is formed in case of the P3HT:PCBM-Al interface. The incorporated Al atoms are expected to be chemically bound and complexed with P3HT.[70] In our case, for the best performing sample S_8, fast annealing and cooling processes were applied. Therefore, a slightly thicker interlayer has formed between the active layer and the Al contact with the assistance of a relatively better movable polymer network and thereby improved Al diffusion, which greatly helps to reduce the contact resistance of the solar cell device. Herein, we can clearly see the importance of the interface between the active layer and the contact. In comparison, the crystallinity and crystal sizes become less influential to the power conversion efficiency, if a certain threshold is passed.

4. CONCLUSION

For the very popular and quite efficient BHJ type solar cell based on P3HT:PCBM a systematic study of the vertical and lateral mesoscopic and molecular structure is performed as a function of the multilayer stack build-up during the solar cell fabrication. Concerning the device function in terms of PCE, the solar cells annealed after the deposition of the aluminum contacts exhibit the best performance (sample S_8). Absence of annealing (sample S_6) or annealing before contact deposition (sample S_7) result both in a significantly worse performance.

The characteristic lateral structure found for P3HT:PCBM on top of glass-ITO-PEDOT:PSS is comparable to structures seen on PEDOT:PSS films without the presence of ITO or on glass/silicon substrates.[54] In contrast, the further assembling of the

Table 2. Determined Parameters for All the Samples from S_1 to S_8 Extracted from Different Measurements Are Listed for Clarity

	S_1	S_2	S_3	S_4	S_5	S_6	S_7	S_8
correlated thickness D_c (nm)	97	96	96	98	95	99	98	99
smallest replicated in-plane length R_c (nm)	261	254	228	207	202	261	261	261
lateral size of ITO (GISAXS) (nm)	105	105	105	105	105	105	105	105
lateral size of P3HT (GISAXS) (nm)				47	63	78	100	65
lateral size of Al (GISAXS) (nm)						95	95	95
efficiency (%)						2.54	1.52	3.61

solar cell, the addition of the top contacts has a clear influence. Structures coarsen during the evaporation of the aluminum contacts, which might be caused by the thermal load applied during this step. For clarity, all parameters extracted in this investigation are summarized in Table 2. In addition, thermal load caused by the top contact deposition can influence the P3HT crystal structure, depending on the sample history, whereas the PCBM crystallites remained unchanged. The overall development of the morphology can explain the main trends in device performance. The highest efficiency is linked with the smallest domain distances, the best crystallinity and the thickest interlayer. The main reason for the relatively poor performance of the preannealed solar cell is the large domain size and the lack of an interlayer. The absence of small domain distances and interlayer as well as low crystallinity, leads to the lowest PCE of only 1.52% for the as-spun solar cell.

In addition, the diffusion of Al atoms to the organic layer and the crystallinity are of importance. The limited ability of Al atoms to diffuse into the crystalline polymer network caused by preannealing leads to a relatively poor connection between the polymer blend layer and the Al contact and a low short circuit current I_{sc}.

Moreover, it needs to be noted that lateral structures are introduced to the solar device by the used ITO bottom electrode, the active P3HT:PCBM layer and the aluminum top contact. The morphology of the aluminum layer is introduced by the phase separation structure of the P3HT:PCBM layer and the growth process of aluminum on the polymer surface.[71] In addition, it is likely that the characteristic lateral structure introduced by the ITO surface roughness influences the lateral structure established in the P3HT:PCBM film. Therefore, smaller ITO domains might be beneficial for a further improvement of the PCE.

AUTHOR INFORMATION

Corresponding Author
*E-mail: muellerb@ph.tum.de. Fax: +49 (0)89 289 12473. Tel: +49 (0)89 289 12451; .

Author Contributions
All authors have given approval to the final version of the manuscript.

Notes
The authors declare no competing financial interest.

REFERENCES

(1) Green, M. A.; Emery, K.; Hishikawa, Y.; Warta, W. *Prog. Photovolt: Res. Appl.* **2011**, *19*, 84−92.
(2) Guo, X.; Li, H.; Ahn, B. Y.; Duoss, E. B.; Hsia, K. J.; Lewis, J. A.; Nuzzo, R. G. *Proc. Natl. Acad. Sci. U.S.A.* **2009**, *106*, 20149−20151.
(3) Lipomi, D. J.; Tee, B. C. K.; Vosgueritchian, M.; Bao, Z. *Adv. Mater.* **2011**, *23*, 1771−1775.
(4) Lee, M. R.; Eckert, R. D.; Forberich, K.; Dennler, G.; Brabec, C. J.; Gaudiana, R. A. *Science* **2009**, *324*, 232−235.
(5) Dennler, G.; Sariciftci, N. S. *IEEE* **2005**, *93*, 1429−1437.
(6) Veenstra, S. C.; Loos, J.; Kroon, J. M. *Prog. Photovolt: Res. Appl.* **2007**, *15*, 727−740.
(7) Lin, Y. Y.; Chen, C. W.; Chu, T. H.; Su, W. F.; Lin, C. C.; Ku, C. H.; Wu, J. J.; Chen, C. H. *J. Mater. Chem.* **2007**, *17*, 4571−4576.
(8) Wang, J. Z.; Zheng, Z. H.; Li, H. W.; Huck, W. T. S.; Sirringhaus, H. *Nat. Mater.* **2004**, *3*, 171−176.
(9) Friend, R. H. *Pure Appl. Chem.* **2001**, *73*, 425−430.
(10) Manigandan, S.; Majumder, S.; Suresh, A.; Ganguly, S.; Kargupta, K.; Banerjee, D. *Sens. Actuators B* **2010**, *144*, 170−175.
(11) Ruderer, M. A.; Müller-Buschbaum, P. *Soft Matter* **2011**, *7*, 5482−5486.
(12) Li, L. G.; Lu, G. H.; Yang, X. N.; Zhou, E. L. *Chin. Sci. Bull.* **2007**, *52*, 148−158.
(13) Günes, S.; Neugebauer, H.; Sariciftci, N. S. *Chem. Rev.* **2007**, *107*, 1324−1338.
(14) Chirvase, D.; Parisi, J.; Hummelen, J. C.; Dyakonov, V. *Nanotechnology* **2004**, *15*, 1317−1323.
(15) Chou, C. H.; Kwan, W. L.; Hong, Z.; Chen, L. M.; Yang, Y. *Adv. Mater.* **2011**, *23*, 1282−1286.
(16) Moule, A. J.; Meerholz, K. *Adv. Funct. Mater.* **2009**, *19*, 1−6.
(17) Kim, Y.; Cook, S.; Tuladhar, S. M.; Choulis, S. A.; Nelson, J.; Durrant, J. R.; Bradley, D. D. C.; Giles, M.; Mcculloch, I.; Ha, C. S.; Ree, M. *Nat. Mater.* **2006**, *5*, 197−202.
(18) Sista, S.; Park, M. H.; Hong, Z.; Wu, Y.; Hou, J.; Kwan, W. L.; Li, G.; Yang, Y. *Adv. Mater.* **2010**, *22*, 380−383.
(19) Mayer, A. C.; Scully, S. R.; Hardin, B. E.; Rowell, M. W.; McGehee, M. D. *Mater. Today* **2007**, *10*, 28−33.
(20) Salim, T.; Wong, L. H.; Bräuer, B.; Kukreja, R.; Foo, Y. L.; Bao, Z.; Lam, Y. M. *J. Mater. Chem.* **2011**, *21*, 242−250.
(21) Pivrikas, A.; Sariciftci, N. S.; Juska, G.; Österbacka, R. *Prog. Photovolt.* **2007**, *15*, 677−696.
(22) Peumans, P.; Yakimov, A.; Forrest, S. R. *Appl. Phys.* **2003**, *93*, 3693−3723.
(23) Brabec, C. J.; Cravino, A.; Meissner, D.; Sariciftci, N. S.; Fromherz, T.; Rispens, M. T.; Sanchez, L.; Hummelen, J. C. *Adv. Funct. Mater.* **2001**, *11*, 374−380.

(24) Yin, W.; Dadmun, M. *ACS Nano* **2011**, *5*, 4756−4768.

(25) Green, M. A.; Emery, K.; Hishikawa, Y.; Warta, W.; Dunlop, E. D. *Prog. Photovolt: Res. Appl.* **2013**, *21*, 827−837.

(26) He, Z.; Zhong, C.; Huang, X.; Wong, W.-Y.; Wu, H.; Chen, L.; Su, S.; Cao, Y. *Adv. Mater.* **2011**, *23*, 4636−4643.

(27) Pandey, R.; Holmes, R. J. *Adv. Funct. Mater.* **2010**, *22*, 5301−5305.

(28) Chen, D.; Liu, F.; Wang, C.; Nakahara, A.; Russell, T. P. *Nano Lett.* **2011**, *11*, 2071−2078.

(29) Parnell, A. J.; Cadby, A. J.; Mykhaylyk, O.; Dunbar, A. D. F.; Hopkinson, P. E.; Donald, A. M.; Jones, R. A. L. *Macromolecules* **2011**, *44*, 6503−6508.

(30) Shao, S.; Liu, J.; Zhang, J.; Zhang, B.; Xie, Z.; Geng, Y.; Wang, L. *ACS Appl. Mater. Interf.* **2012**, *4*, 5704−5710.

(31) Kim, M.-S.; Kim, B.-G.; Kim, J. *ACS Appl. Mater. Interfaces* **2009**, *1*, 1264−1269.

(32) Chen, D.; Nakahara, A.; Wie, D.; Nordlund, D.; Russell, T. P. *Nano Lett.* **2011**, *11*, 561−567.

(33) Tillack, A. F.; Noone, K. M.; Macleod, B. A.; Nordlund, D.; Nagle, K. P.; Bradley, J. A.; Hau, S. K.; Lip, H.-L.; Jen, A. K.-Y.; Seidler, G. T.; Ginger, D. S. *ACS Appl. Mater. Interfaces* **2011**, *3*, 726−732.

(34) Perlich, J.; Memesa, M.; Diethert, A.; Metwalli, E.; Wang, W.; Roth, S. V.; Timmann, A.; Gutmann, J. S.; Müller-Buschbaum, P. *ChemPhysChem* **2009**, *10*, 800−806.

(35) Shaheen, S. E.; Brabec, C. J.; Sariciftci, N. S.; Padinger, F.; Fromherz, T.; Hummelen, J. C. *Appl. Phys. Lett.* **2001**, *78*, 841−843.

(36) Huang, Y.-C.; Tsao, C.-S.; Chuang, C.-M.; Lee, C.-H.; Hsu, F.-H.; Cha, H.-C.; Chen, C.-Y.; Lin, T.-H.; S, C.-J.; J, U.-S.; S, W.-F. *J. Phys. Chem. C* **2012**, *116*, 10238−10244.

(37) Dennler, G.; Scharber, M. C.; Brabec, C. J. *Adv. Funct. Mater.* **2009**, *21*, 1325−1338.

(38) Maradalen, J.; Samuelsen, E. J.; Gautun, O. R.; Carlsen, P. H. *Solid State Commun.* **1991**, *77*, 337−339.

(39) Sista, S.; Park, M.-H.; Hong, Z.; Wu, Y.; Hou, J.; Kwan, W. L.; Li, G.; Yang, Y. *Adv. Mater.* **2010**, *22*, 380−382.

(40) Kingsley, J. W.; Green, A.; Lidzey; D. G.. *Proc. SPIE* **2009**, *7416*, 74160T.

(41) Meier, R.; Birkenstock, C.; Palumbiny, C. M.; Müller-Buschbaum, P. *Phys. Chem. Chem. Phys.* **2012**, *14*, 15088−15098.

(42) Roth, S. V.; Döhrmann, R.; Dommach, M.; Kuhlmann, M.; Kröger, I.; Gehrke, R.; Walter, H.; Schroer, C.; Lengeler, B.; Müller-Buschbaum, P. *Rev. Sci. Instrum.* **2006**, *77*, 085106−1- 085106−6.

(43) Müller-Buschbaum, P. Springer: Berlin, 2009, *776*, 61−89.

(44) Perlich, J.; Rubeck, J.; Botta, S.; Gehrke, R.; Roth, S. V.; Ruderer, M. A.; Prams, S. M.; Rawolle, M.; Zhong, Q.; Körstgens, V.; Müller-Buschbaum, P. *Rev. Sci. Instrum.* **2010**, *81*, 105105−1-105105−7.

(45) Sirringhaus, H.; Brown, P. J.; Friend, R. H.; Nielsen, M. M.; Bechgaard, K.; Langeveld-Voss, B. M. W.; Spiering, A. J. H.; Janssen, R. A. J.; Meijer, E. W.; Herwig, P.; de Leeuw, D. M. *Nature* **1999**, *401*, 685−688.

(46) Shrotriya, V.; Li, G.; Yao, Y.; Moriarty, T.; Emery, K.; Yang, Y. *Adv. Funct. Mater.* **2006**, *16*, 2016−2023.

(47) Müller-Buschbaum, P.; Gutmann, J. S.; Lorenz, C.; Schmitt, T.; Stamm, M. *Macromolecules* **1998**, *31*, 9265−9268.

(48) Yoneda, Y. *Phys. Rev.* **1963**, *131*, 2010−2013.

(49) Müller-Buschbaum, P.; Stamm, M. *Macromolecules* **1998**, *31*, 3686−3692.

(50) Kaune, G.; Metwalli, E.; Meier, R.; Körstgens, V.; Schlage, K.; Couet, S.; Röhlsberger, R.; Roth, S. V.; Müller-Buschbaum, P. *ACS Appl. Mater. Interfaces* **2011**, *3*, 1055−1062.

(51) Blom, P. W. M.; Mihailetchi, V. D.; Koster, L. J. A.; Markow, D. E. *Adv. Mater.* **2007**, *19*, 1551−1566.

(52) Girotto, C.; Moia, D.; Rand, B. P.; Heremans, P. *Adv. Funct. Mater.* **2011**, *21*, 64−72.

(53) Huang, Y.-C.; Chia, H.-C.; Chuang, C.-M.; Tsao, C.-S.; Chen, C.-Y.; Su, W.-F. *Sol. Energy Mater. Sol. Cells* **2013**, *114*, 24−30.

(54) Ruderer, M. A.; Guo, S.; Meier, R.; Chiang, H.-Y.; Körstgens, V.; Wiedersich, J.; Perlich, J.; Roth, S. V.; Müller-Buschbaum, P. *Adv. Funct. Mater.* **2011**, *21*, 3382−3391.

(55) Thompson, B. C.; Fréchet, J. M. J. *Angew. Chem., Int. Ed.* **2008**, *47*, 58−77.

(56) Müller-Buschbaum, P. *Anal. Bioanal. Chem.* **2003**, *376*, 3−10.57.

(57) Wu, W. R.; Jeng, U. S.; Su, C. J.; Wei, K. H.; Su, M. S.; Chiu, M. Y.; Chen, C. Y.; Su, W. B.; Su, C. H.; Su, A. C. *ACS Nano* **2011**, *5*, 6233−6243.

(58) Lin, T. L.; Jeng, U. S.; Tsao, C. S.; Liu, W. J.; Canteenwala, T.; Chiang, L. Y. *J. Phys. Chem. B* **2004**, *108*, 14884−14888.

(59) Liao, H.-C.; Tsao, C.-S.; Lin, T.-H.; Chuang, C.-M.; Chen, C.-Y.; Jeng, U.-S.; Su, C.-H.; Chen, Y.-F.; Su, W.-F. *J. Am. Chem. Soc.* **2011**, *133*, 13064−13073.

(60) Erb, T.; Zhokhavets, U.; Gobsch, G.; Raleva, S.; Stühn, B.; Schilinsky, P.; Waldauf, C.; Brabec, C. J. *Adv. Funct. Mater.* **2005**, *15*, 1193−1196.

(61) Gutmann, J. S.; Müller-Buschbaum, P.; Stamm, M. *Farady Disc.* **1999**, *112*, 285−297.

(62) Müller-Buschbaum, P.; Gutmann, J. S.; Stamm, M. *Phys. Chem. Chem. Phys.* **1999**, *1*, 3857−3863.

(63) Chen, W.; Nikiforov, M. P.; Darling, S. B. *Energy Environ. Sci.* **2012**, *5*, 8045−8050.

(64) Ruderer, M. A.; Metwalli, E.; Wang, W.; Kaune, G.; Roth, S. V.; Müller-Buschbaum, P. *Chem.Phys.Chem.* **2009**, *10*, 664−671.

(65) Agostinelli, T.; Lilliu, S.; Labram, J. G.; Campoy-Quiles, M.; Hampton, M.; Pires, E.; Rawle, J.; Bikondoa, O.; Bradley, D. D. C.; Anthopoulos, T. D.; Nelson, J.; Macdonald, J. E. *Adv. Funct. Mater.* **2011**, *21*, 1701−1708.

(66) Ng, A.; Liu, X.; To, C. H; Djurišić, A. B; Zapien, J. A; Chan, W. K. *ACS Appl. Mater. Interfaces* **2013**, *5*, 4247−4259.

(67) Yu, C.-Y.; Jen, T.-J.; Chen, S.-A. *ACS Appl. Mater. Interfaces* **2013**, *5*, 4086−4092.

(68) Kim, H. J.; Lee, H. H.; Kim, J.-J. *Macromol. Rapid Commun.* **2009**, *30*, 1269−1273.

(69) Kim, H. J.; Park, J. H.; Lee, H. H.; Lee, D. R.; Kim, J.-J. *Org. Electron.* **2009**, *10*, 1505−1510.

(70) Dannetun, P.; Boman, M.; Stafström, S.; Salaneck, W. R.; Lazzaroni, R.; Fredriksson, C.; Bredas, J. L.; Zamboni, R.; Taliani, C. *J. Chem. Phys.* **1993**, *99*, 664−672.

(71) Kumar, A.; Li, G.; Hong, Z.; Yang, Y. *Nanotechnology* **2009**, *20*, 1−3.